Synthesis and mechanistic insights of $SiO_2@WO_3@Fe_3O_4$ as a Novel Supported Photocatalyst for Wastewater Remediation under Visible Light

Ander Diego-Lopez, Oscar Cabezuelo, Alejandro Vidal-Moya, M. Luisa Marin [*], Francisco Bosca [*]

Instituto de Tecnología Química (UPV-CSIC), Universitat Politècnica de València-Consejo Superior de Investigaciones Científicas, Avda. de los Naranjos s/n, València, 46022, Spain

ARTICLE INFO

ABSTRACT

A new optimized photocatalyst for wastewater remediation at neutral pH has been developed and fully characterized. The catalyst features microparticles of SiO_2 as a supporting substrate and a uniform shell of WO_3 nanoparticles externally decorated with Fe_3O_4 nanocrystals. The photocatalytic activity of $SiO_2@WO_3@Fe_3O_4$ was evaluated and compared to its $SiO_2@WO_3$ counterpart on the photodegradation of methylene blue (MB) under visible light, with and without H_2O_2. Best results were obtained for $SiO_2@WO_3@Fe_3O_4$ in the presence of H_2O_2, whose potential for wastewater remediation was further evaluated on the photodegradation and mineralization of a contaminant of emerging concern such as diclofenac (DCF). Furthermore, a photocatalytic mechanism was proposed based on the performed electron paramagnetic resonance (EPR) experiments, which provided evidence for the intermediates generated in all the involved photocatalytic processes. Hence it was proven that ·OH is the species responsible for the photocatalyzed oxidation of MB and DCF. The generation of ·OH is boosted by a synergistic effect between Fe_3O_4 and WO_3 in the presence of light and H_2O_2.

1. Introduction

The intensive exploitation of agriculture, together with the rapid industrial development, are the main causes of surface and groundwater pollution, which lead to a decrease in freshwater availability, one of the biggest problems that society is facing today [1]. In this context, the presence of pharmaceutical compounds in water is particularly threatening due to their toxicity and the uncertainty of the extent of the problems they could arise [2]. Among them, diclofenac (DCF), a non-steroidal anti-inflammatory drug, is one of the most frequently detected compounds in aquatic environments, and its ecotoxicity, especially in the presence of other organic contaminants and metals, has been demonstrated [3–5]. However, conventional wastewater treatments are not able to effectively eliminate DCF, with reported degradation efficiencies of less than 10 % [6]. In consequence, it becomes crucial to develop efficient technologies able to remove contaminants of emerging concern (CECs) like DCF from the aquatic media, allowing water reuse.

Advanced Oxidation Processes (AOPs), which are characterized by the production of hydroxyl radical (·OH), are presented as promising technologies for the oxidation of organic pollutants. Among AOPs, heterogeneous photocatalysis and specifically semiconductor-based photocatalysis, have been widely reported as a viable option for wastewater decontamination [7,8]. Thus, the absorption of photons with the appropriate energy by the semiconductor can stimulate an electron transfer process from the valence band (VB) to the conduction band (CB) on the semiconductor surface, generating a photo-excited electron-hole pair (e^-—h^+). From the photo-generated e^-, species such as superoxide anion ($O_2^{·-}$) can be produced, while the photo-generated h^+ could be able to produce hydroxyl radical (·OH) [9,10].

In this context, TiO_2 has been the most widely studied material for photocatalytic applications due to its low cost, chemical and photochemical corrosion stability, and nontoxicity. However, it displays several drawbacks, such as a low photocatalytic quantum yield due to its fast e^-—h^+ pair recombination process or the impossibility of using visible light due to its band gap (3.2 eV) [11,12]. For that reason, other semiconductors, such as tungsten trioxide (WO_3), are gaining momentum in the field of photocatalysis for environmental applications. Among its advantages, WO_3 performs efficient photocatalytic processes under visible light (band gap between 2.6-2.8 eV) [13–15].

Nevertheless, its band edge (*ca.* +0.5 V *vs* NHE) prevents the production of $O_2^{\cdot-}$, and consequently, the electron in the CB rapidly tends to recombine with the h^+ in the VB, inhibiting the generation of ·OH [15]. Therefore, different studies using WO_3 as a semiconductor have been performed to overcome its disadvantages [16–30]. In this sense, the photoreactivity of WO_3 has been improved by the presence of electron scavengers, such as H_2O_2 or Fe^{3+}. These inorganic oxidants, acting as electron acceptors, would rapidly react with the photogenerated electrons in the CB of WO_3 and consequently prevent recombination with the holes [17,25,28]. Nevertheless, coupling WO_3 with other low band gap semiconductors has resulted in being one of the most promising ways to reduce the $e^-—h^+$ pair recombination due to the charge migration between semiconductors [16,18,20–24,29–31]. In this context, recent studies have demonstrated a better photocatalytic activity of new hybrid photocatalysts containing WO_3 and Fe_2O_3 or Fe_3O_4 than the pristine semiconductors. Even more, improved water decontamination has been observed using H_2O_2 with $WO_3@Fe_3O_4$ nanopowders under acidic conditions (pH *ca.* 2.8) or with nanocomposites formed by mixing magnetite nanoparticles and WO_3 nanorods [18,23]. Nevertheless, although other studies have shown that Fe_3O_4 nanoparticles are able to perform photo-Fenton oxidations in the presence of H_2O_2 [32], ambiguous explanations for the better photocatalytic activity of $WO_3@Fe_3O_4$ nanocomposites have been provided in all cases [16,18, 20,21,23,24,29].

Another interesting point about photocatalysts based on semiconductors is that there are only a few cases in which they have been synthesized on supporting substrates, even though it offers advantages, such as the easier separation from the reaction medium or the prevention of the aggregation of the nanocrystals [33]. In this sense, although $WO_3@Fe_3O_4$ photocatalysts have been used for water decontamination in batch reactors applying magnetic fields for separating and recovering this type of powder catalyst particles, no supported photocatalytic systems based on $WO_3@Fe_3O_4$ have been reported.

With this background, the aim of the present work was to design a supported photocatalyst based on WO_3 with improved oxidant properties for wastewater remediation at neutral pH. In this context, microparticles of SiO_2 were selected as the support of the WO_3 photocatalysts because they are cheap, easily available, offer high mechanical stability, and are transparent in the light spectral range where WO_3 will be excited. Thereby, after the synthesis of $SiO_2@WO_3@Fe_3O_4$ and an extensive characterization, the photocatalytic activity of $SiO_2@WO_3@Fe_3O_4$ and $SiO_2@WO_3$ (synthesized as a control) will be evaluated and compared in the presence and in the absence of H_2O_2, using methylene blue (MB) as a model contaminant. Furthermore, the reuse of the new supported photocatalyst will be demonstrated. Moreover, the potential of this new photocatalyst for water remediation will be tested against DCF, as a CEC, in the presence of H_2O_2. Finally, a deep mechanistic insight based on electron paramagnetic resonance (EPR) measurements, together with the photocatalytic results, will allow the postulation of plausible reaction mechanisms.

2. Materials and methods

2.1. Chemicals

Tetraethyl orthosilicate (TEOS), ammonium hydroxide (28-32%, NH_4OH), ammonium metatungstate (AMT), ferrous chloride tetrahydrate ($FeCl_2 \cdot 4H_2O$), ferric chloride anhydrous ($FeCl_3$), methylene blue (MB) and hydrogen peroxide (50%, H_2O_2) were purchased from Sigma Aldrich. 5,5-dimethyl-1-pyrroline-N-oxide (DMPO) was purchased from TCI chemicals. Tungsten (VI) chloride (WCl_6) was purchased from Fisher Scientific. Methanol (MeOH) and ethanol (EtOH) were purchased from Scharlab.

2.2. Synthesis and characterization

2.2.1. Synthesis of SiO₂ spheres

SiO_2 spheres were synthesized following the Stöber method [34]. Thus, TEOS (269 mmol) was added to a solution of NH_4OH (2.11 mmol) in EtOH (1500 mL) at 0°C. After two hours under these conditions, the reaction was conducted at 22°C for further 24 hours. Then, the SiO_2 particles were centrifuged (4000 rpm for 5 min) and washed with EtOH (200 mL). The obtained SiO_2 particles were dried under vacuum.

2.2.2. Synthesis of Fe₃O₄ nanoparticles

Magnetite (Fe_3O_4) nanoparticles were synthesized *via* a co-precipitation method [35]. Thus, $FeCl_2 \cdot 4H_2O$ (11.8 mmol) and $FeCl_3$ (18.5 mmol) were dissolved in distilled H_2O (100 mL) under a nitrogen gas flow at 50°C. After 45 minutes under vigorous stirring, NH_4OH (260 mmol) was added to the mixture, which was stirred at the same conditions for further 2 hours. Finally, the obtained Fe_3O_4 nanoparticles were washed with water, centrifuged (3500 rpm for 15 min), washed with EtOH, and finally centrifuged (5000 rpm for 5 min). The obtained Fe_3O_4 nanoparticles were dried under vacuum.

2.2.3. Synthesis of SiO₂@WO₃ photocatalyst

A suspension of the synthesized SiO_2 particles (500 mg) in EtOH (24 mL) was prepared under sonication. In parallel, a mixture of WCl_6 (1.56 mmol) and EtOH (40 mL) was sonicated prior to its addition dropwise to the SiO_2 suspension under vigorous stirring at room temperature. After 2 hours, the suspension was submitted to a humidified airflow of 100 mL min^{-1} for 20 h at room temperature and then centrifuged to obtain a precipitate which was washed several times with water and ethanol and centrifuged (3500 rpm for 15 minutes). The obtained microparticles were dried under vacuum overnight, prior to calcination (500 °C for 3 hours with a calcination ramp of 57 °C h^{-1}), giving rise to the $SiO_2@WO_3$ photocatalyst.

2.2.4. Synthesis of SiO₂@WO₃@Fe₃O₄ photocatalyst

$SiO_2@WO_3@Fe_3O_4$ photocatalyst was synthesized using the previously synthesized Fe_3O_4 nanoparticles and $SiO_2@WO_3$ microparticles. Thus, an aqueous ammonium metatungstate (AMT) solution (1 mM, 6.5 mL) was added dropwise to $SiO_2@WO_3$ (650 mg) under vigorous stirring. After 45 minutes at room temperature, Fe_3O_4 nanoparticles (27.1 mg) were added, and the reaction was stirred for further 15 hours. Then, the suspension was centrifuged, and the obtained precipitate was washed with water (3000 rpm for 15 minutes) and with ethanol (3000 rpm for 15 minutes). The obtained $SiO_2@WO_3@Fe_3O_4$ photocatalyst was dried under vacuum.

2.2.5. Characterization

All the instrumentation employed is described in Section 2 of SI.

2.3. Photocatalytic activity

The photocatalytic activity of the synthesized $SiO_2@WO_3$ and $SiO_2@WO_3@Fe_3O_4$ photocatalysts was evaluated using MB as a model organic contaminant. An LZC-4V photoreactor from Luzchem Research Inc. was used to perform the photocatalytic degradation experiments, using 8 lamps of 8 W with λ_{em} centered at *ca.* 420 nm. Samples were placed in the center of the photoreactor where the light intensity was *ca.* 3.8×10^{-3} W cm^{-2}, measured with a radiometer (P-2110, Gigahertz-Optik with radiometric detector head RW-3705-5). MB degradation was determined by UV-Vis analysis using a Cary 60 UV-Vis spectrophotometer from Agilent Technologies.

Thus, photocatalytic degradations of MB were performed by adding 12 mg of $SiO_2@WO_3$ or $SiO_2@WO_3@Fe_3O_4$ to 12 mL of MB (6×10^{-5} M) aqueous solutions with and without H_2O_2 (4.4 mM). The reaction mixtures were adjusted to pH 7 using NaOH (1 M). Each assay was performed keeping the aqueous mixture under stirring in the dark for 30
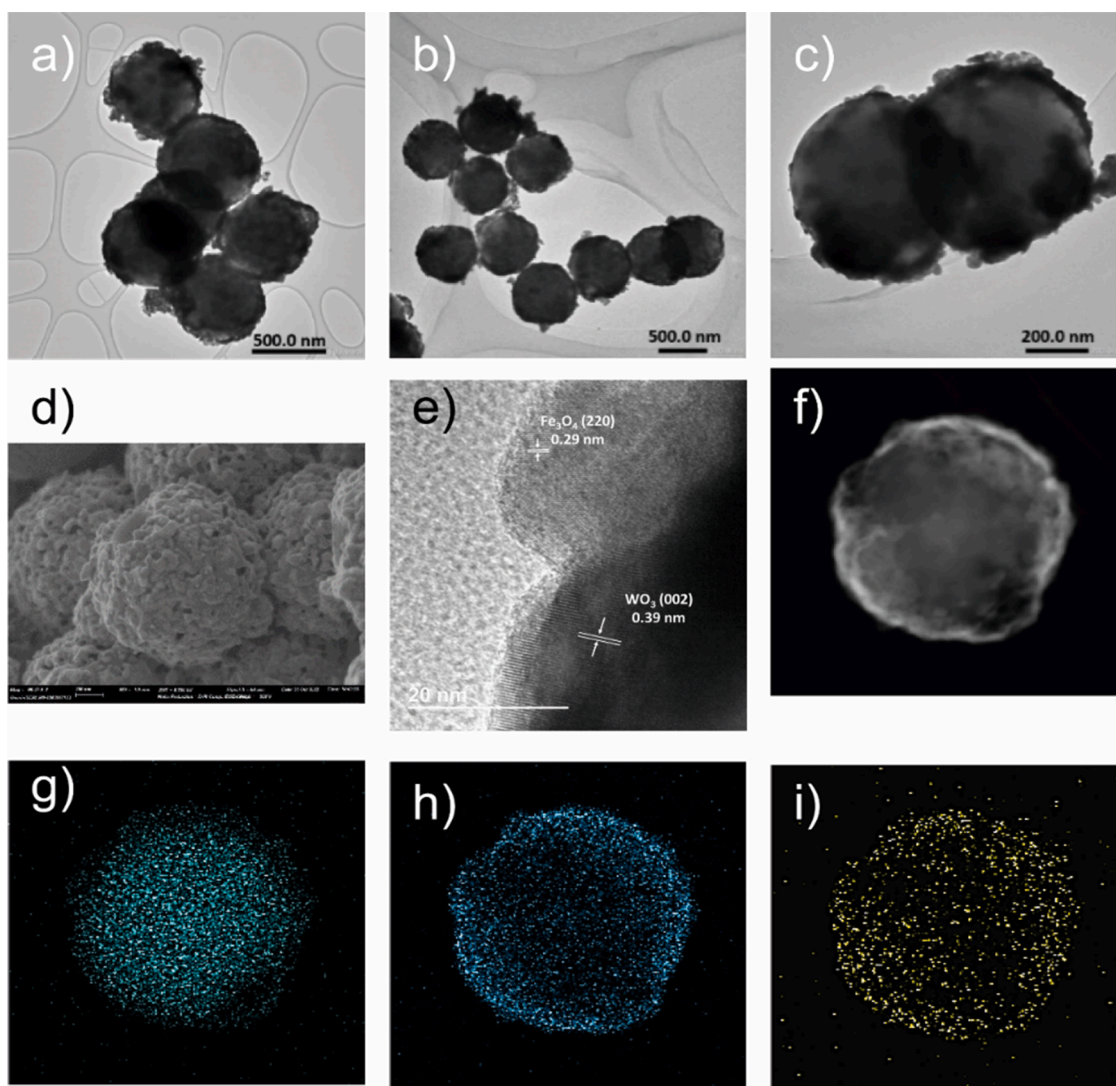
Figure 1. TEM images of: (a) SiO$_2$@WO$_3$ photocatalyst and (b-c) SiO$_2$@WO$_3$@Fe$_3$O$_4$ photocatalyst. (d) FESEM image of SiO$_2$@WO$_3$@Fe$_3$O$_4$ photocatalyst. (e) HRTEM image of WO$_3$ and Fe$_3$O$_4$ lattices in SiO$_2$@WO$_3$@Fe$_3$O$_4$ photocatalyst. (f) STEM dark field image of SiO$_2$@WO$_3$@Fe$_3$O$_4$ photocatalyst and its elemental mapping of Si (g), W (h), and Fe (i) by EDS analysis.

minutes prior to irradiation, to reach the adsorption/desorption equilibrium. To monitor the progress of the photoreactions, aliquots of 500 μL were taken at different times. Prior to the analysis of the samples, they were mixed with methanol (2 mL) and stirred for 15 minutes to recover the adsorbed MB from the photocatalyst surface, and then filtered with a CLARIFY-PTFE 13 mm syringe filter with 0.45 μm porous. Finally, the MB degradation was determined by UV-Vis analysis.

The reusability of the SiO$_2$@WO$_3$@Fe$_3$O$_4$ photocatalyst was assessed in consecutive photodegradation of aqueous MB solutions (6×10^{-5} M) in the presence of H$_2$O$_2$. After each cycle, the reaction mixture was centrifuged, and the photocatalyst was washed several times with water and ethanol, centrifuged (3500 rpm for 15 minutes), and dried overnight under vacuum.

Finally, the activity of SiO$_2$@WO$_3$@Fe$_3$O$_4$ was tested on the photodegradation and mineralization of DCF. Thus, an aqueous DCF solution (1.5×10^{-4} M) was irradiated in the presence of SiO$_2$@WO$_3$@Fe$_3$O$_4$ (1 mg mL^{-1}) and H$_2$O$_2$ (1.1×10^2 M) under the same conditions as the above mentioned. The progress of the photoreactions was monitored by taking aliquots of 200 μL at different times. Prior to the analysis of the samples, they were mixed with 1.8 mL of an aqueous solution containing 4-nitrobenzoic acid (1×10^{-4} M). After filtering the samples with a CLARIFY-PTFE 13 mm syringe filter with 0.45 μm porous, samples were

submitted to UPLC analysis. A C18 column (2.1 × 50 mm, 1.7 μm particle size) was employed for the UPLC studies. The mobile phase was fixed at 0.5 mL min^{-1} with an isocratic mixture of a 0.1 % aqueous formic acid solution (50 %) and acetonitrile (50 %). Aliquots of 5 μL were injected, and the detection wavelength was fixed at 277 nm. Additionally, the mineralization was monitored via total organic carbon using a Shimadzu TOC-L total organic carbon analyzer.

2.4. Electron Paramagnetic Resonance (EPR) tests

For detection of ·OH, 1 mg mL^{-1} aqueous suspensions of SiO$_2$@WO$_3$ or SiO$_2$@WO$_3$@Fe$_3$O$_4$ were prepared in the presence of DMPO (10 mM), with and without H$_2$O$_2$ (4.4 mM). In parallel, for the detection of O$_2$·$^{-}$, suspensions of SiO$_2$@WO$_3$ or SiO$_2$@WO$_3$@Fe$_3$O$_4$ (1 mg mL^{-1}) in the presence of DMPO (10 mM) were prepared in EtOH:H$_2$O (4:1). Afterwards, the EPR spectra were recorded in a flat cell, in darkness, and after one-minute irradiation.

2.5. Photoluminescence emission measurements

For the photoluminescence emission studies, samples of SiO$_2$@WO$_3$, SiO$_2$@WO$_3$@Fe$_3$O$_4$, and Fe$_3$O$_4$ were placed in flat quartz 0.1 cm
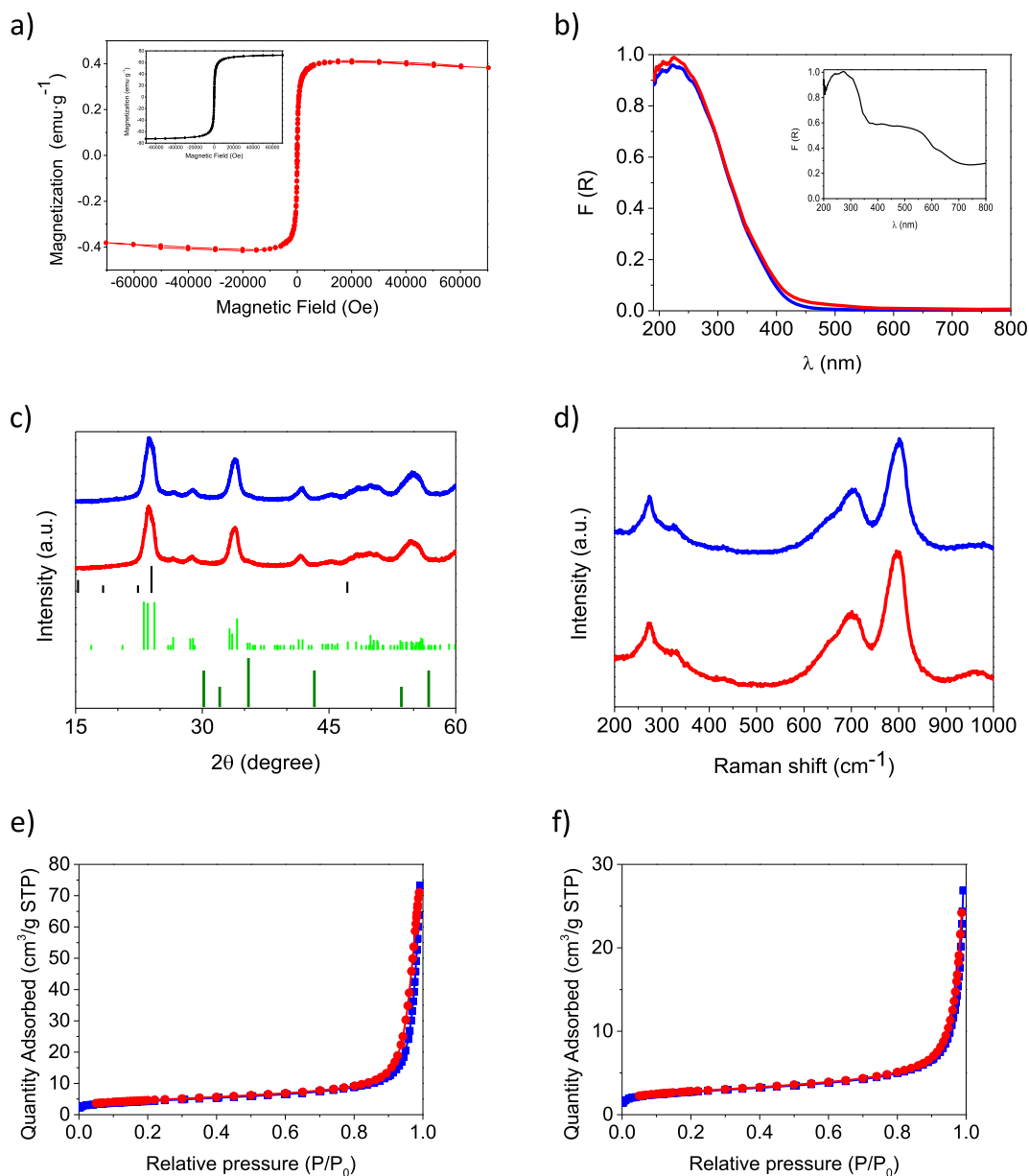
Figure 2. (a) Magnetization curve of $SiO_2@WO_3@Fe_3O_4$ photocatalyst. Inset: results obtained for pure Fe_3O_4 nanoparticles. (b) DR spectra of $SiO_2@WO_3$ (blue) and $SiO_2@WO_3@Fe_3O_4$ (red) photocatalysts. Inset: results obtained for pure Fe_3O_4 nanoparticles. (c) XRD patterns of $SiO_2@WO_3$ (blue) and $SiO_2@WO_3@Fe_3O_4$ (red) with references of SiO_2 (black), WO_3 (green), and Fe_3O_4 (olive). (d) Raman spectra of $SiO_2@WO_3$ (blue) and $SiO_2@WO_3@Fe_3O_4$ (red) photocatalysts. N_2 adsorption-desorption isotherms of (e) $SiO_2@WO_3$ and (f) $SiO_2@WO_3@Fe_3O_4$ photocatalysts.

cuvettes.

3. Results and discussion

3.1. Characterization of the novel photocatalyst

A scheme illustrating the synthesis of the photocatalysts can be found in SI, section S1. Two new photocatalysts were synthesized using the same homemade supporting silica substrate (SiO_2 microparticles with a diameter size of 598 ± 22 nm, see Figures S3a and S4a). TEM analysis reveals that the nanocrystal shell of WO_3 is homogeneously distributed over the surface of SiO_2 cores, resulting in $SiO_2@WO_3$ microparticles with a rough surface and increased diameter (673 ± 31 nm, see Figure 1a and S4c). A WO_3 thin shell of *ca.* 37 nm was determined from the diameter difference between SiO_2 and $SiO_2@WO_3$. Furthermore, based on the diameters and estimated density of both SiO_2 and

$SiO_2@WO_3$ particles, a 53 % (w/w) WO_3 in $SiO_2@WO_3$ was calculated (see more details in section S4 of SI), while an experimental value of 30 % of WO_3 (w/w) was found from ICP-OES analysis. The smaller value found from the ICP analysis clearly indicates that the WO_3 shell is formed by nanocrystals with small gaps.

The previously synthesized Fe_3O_4 nanoparticles (see Figure S1 and S3b), which showed a diameter size of *ca.* 12 ± 2 nm (Figure S4b), were used to decorate $SiO_2@WO_3$ microspheres in order to get $SiO_2@WO_3@Fe_3O_4$ photocatalyst (see synthesis procedure in Figure S2 and TEM images in Figure 1b,c). This new material shows a particle diameter increased up to 680 ± 30 nm (Figure S4d), keeping a rough texture quite similar to the observed for $SiO_2@WO_3$. Moreover, this diameter value is indicative that a monolayer of magnetite nanocrystals would partially cover the $SiO_2@WO_3$ microspheres. The FESEM analysis also shows the rough texture of the surface of $SiO_2@WO_3@Fe_3O_4$ photocatalyst, which is composed of small nanocrystals of WO_3 and Fe_3O_4 (see Figure 1d).
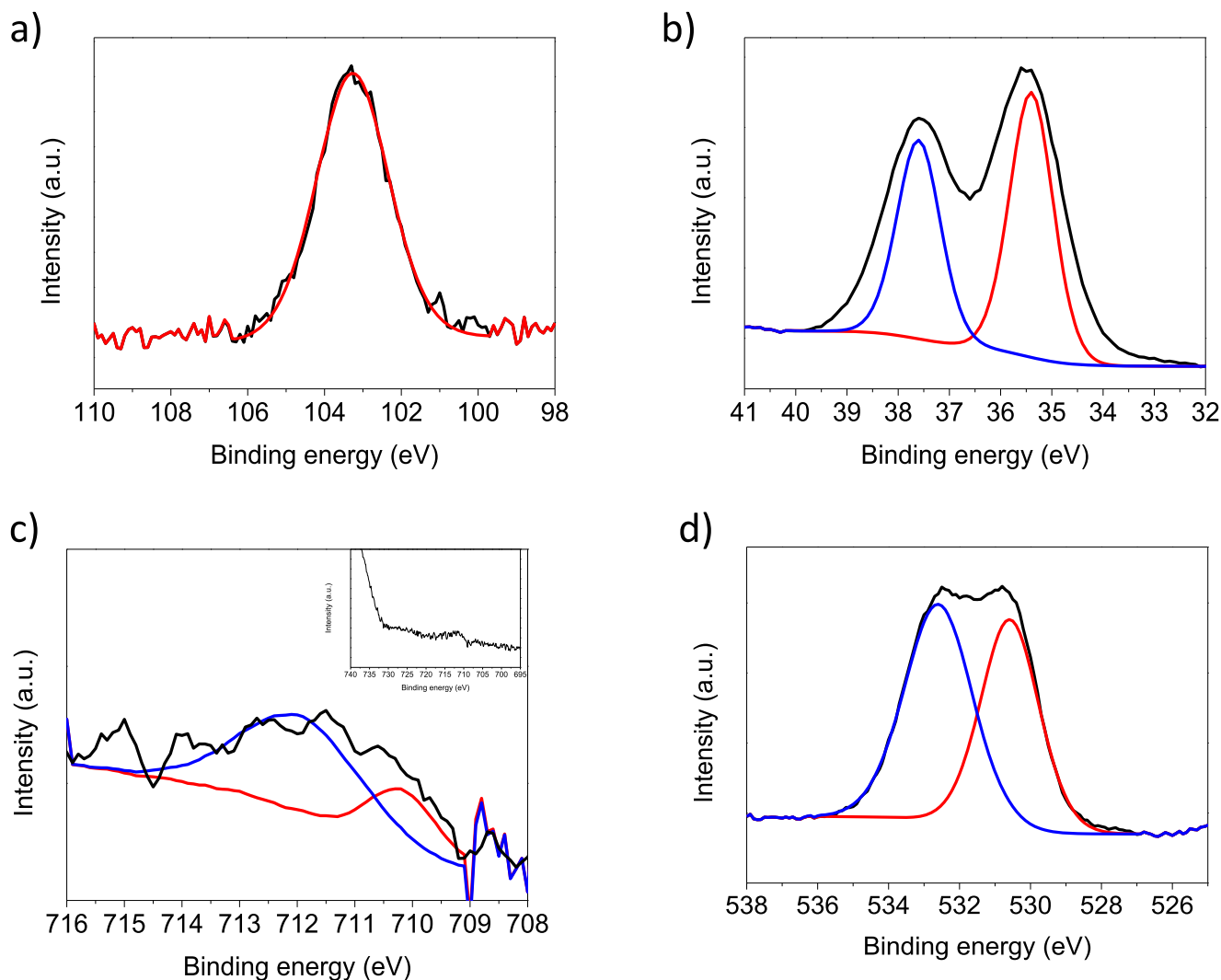
Figure 3. High-resolution XPS spectra of Si2p (a), W4f (b), Fe2p$_{3/2}$ (c), and O1s (d) in SiO$_2$@WO$_3$@Fe$_3$O$_4$ photocatalyst. Inset (c): complete Fe2p spectra.

Moreover, a high-resolution TEM (HRTEM) image of SiO$_2$@WO$_3$@Fe$_3$O$_4$ (Figure 1e) shows the junction between WO$_3$ and Fe$_3$O$_4$. A more careful analysis of the interplanar crystal distances shows a value of 0.39 nm for WO$_3$ and 0.29 nm for Fe$_3$O$_4$, which correspond to the (002) and (220) crystal planes, respectively [36,37]. Furthermore, the SAED pattern of WO$_3$ crystals on SiO$_2$@WO$_3$@Fe$_3$O$_4$ photocatalyst was also analyzed to further investigate the crystallinity of the material (Figure S4). Thus, the polycrystal analysis (Figure S5a) shows the presence of (002), (202), (140), and (420) planes of monoclinic WO$_3$ (JCPDS No. 00-043-1035). Single crystal analysis shows the presence of two planes with d spacings of 0.37 nm and 0.36 nm, which correspond to the (002) and (200) planes of the monoclinic phase, respectively (Figure S5b) [38].

Moreover, the STEM-EDS elemental mapping displays a homogeneous distribution of WO$_3$ and Fe$_3$O$_4$ on the coating shell of SiO$_2$@WO$_3$@Fe$_3$O$_4$ (Figure 1f-i). This result was confirmed by SEM-EDS analysis (see Figure S6). The STEM-EDS elemental analysis also revealed 41% of WO$_3$ and 8% of Fe$_3$O$_4$ (w/w) in SiO$_2$@WO$_3$@Fe$_3$O$_4$. Although the values obtained from STEM-EDS must be used with caution because they are only an estimation [39], this percentage of magnetite is compatible with the amount of Fe$_3$O$_4$ nanoparticles that would produce an increase in the diameter size of SiO$_2$@WO$_3$ of *ca.* 6 nm.

The magnetization saturation of Fe$_3$O$_4$ and SiO$_2$@WO$_3$@Fe$_3$O$_4$ was determined at 300 K for the evaluation of the magnetic response to an external field (see Figure 2a). Thus, Fe$_3$O$_4$ and SiO$_2$@WO$_3$@Fe$_3$O$_4$

presented values of 72.5 and 0.4 emu g^{-1}, respectively. Magnetization saturation of Fe$_3$O$_4$ nanoparticles agreed with the values described for magnetite nanocrystals of sizes ca. 12 nm [40]. Therefore, after adding SiO$_2$@WO$_3$, a substantial decrease in the magnetic properties of the samples was observed. This behavior can be mainly attributed to the increase in the mass caused by the addition of SiO$_2$@WO$_3$.

Diffuse reflectance spectra (DRS) were performed for both photocatalysts and for Fe$_3$O$_4$ nanoparticles (Figure 2b). The Fe$_3$O$_4$ incorporation to the WO$_3$ shell structure produces a slight red shift on the diffuse reflectance spectrum, improving the visible-light harvesting capability of the SiO$_2$@WO$_3$@Fe$_3$O$_4$ photocatalyst compared to SiO$_2$@WO$_3$, reaching *ca.* 700 nm. Furthermore, the band-gap energy for both composites was calculated through the Kubelka-Munk function and the Tauc plot method [41] and resulted in being lower for SiO$_2$@WO$_3$@Fe$_3$O$_4$ (2.77 eV) than for SiO$_2$@WO$_3$ (2.87 eV) (Figure S7). Those values are in concordance with the reported band gap for WO$_3$ [17,42].

SiO$_2$@WO$_3$ and SiO$_2$@WO$_3$@Fe$_3$O$_4$ XRD patterns (Figure 2c) showed broad peaks at 2θ = 23.7°, 26.5°, 28.9°, 33.9°, 41.7° and 55.0°, which, as demonstrated previously from the SAED analysis, could be attributed to the monoclinic phase of WO$_3$ [43]. However, the small size of the WO$_3$ crystals clustered in the coating shell can lead to the broadly observed signals, which are coherent with the XRD pattern for the monoclinic WO$_3$ (JCPDS No. 00-043-1035). In fact, the WO$_3$ crystal size was averaged over *ca.* 6.5 nm through the Scherrer equation, where the diffraction peak at 2θ = 23.6° was used for the crystal size estimation.
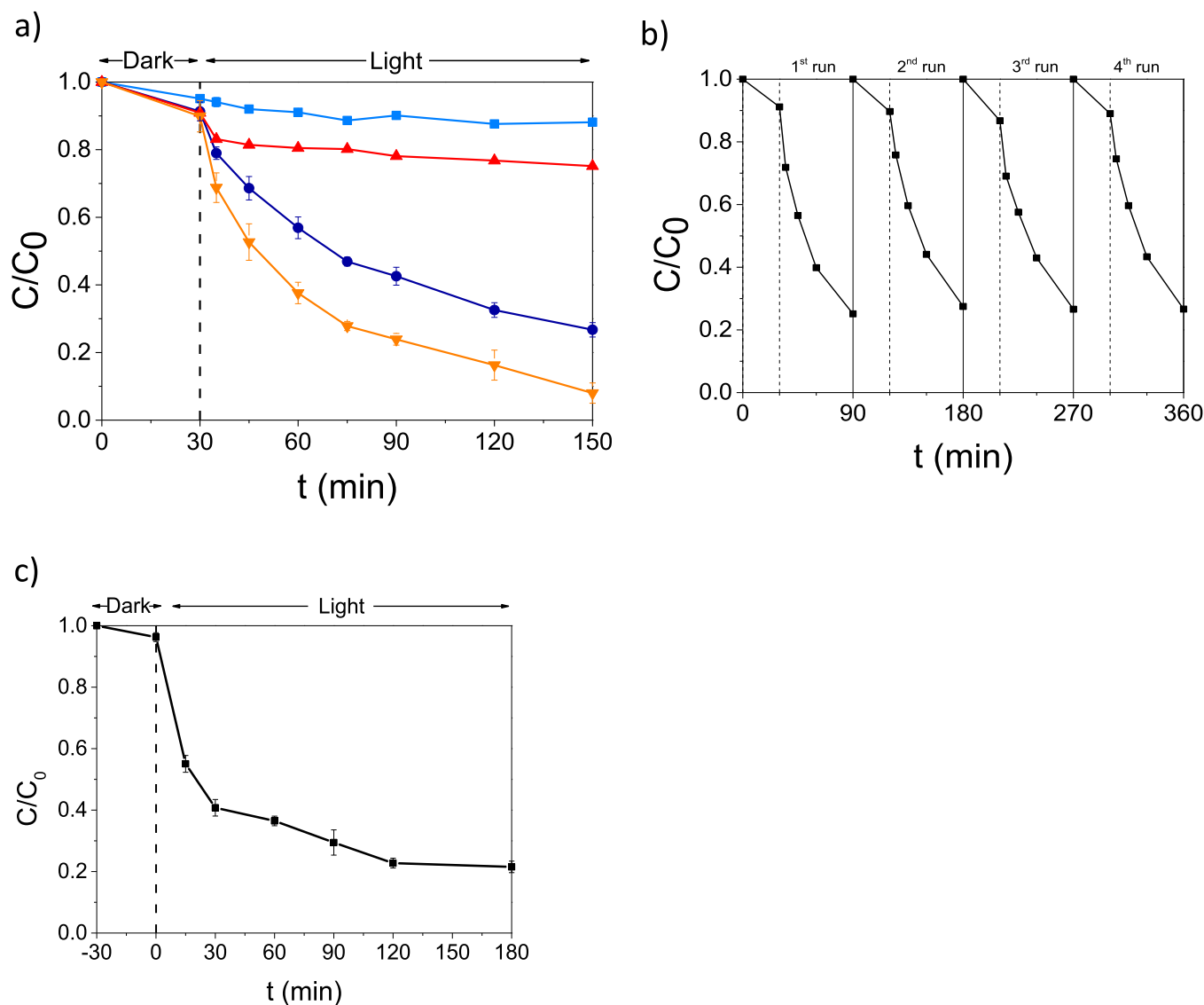
Figure 4. (a) Degradation of an aqueous MB solution (6×10^{-5} M) under visible-light irradiation (8 lamps of λ_{em} *ca.* 420 nm) in the presence of 1 mg mL^{-1} of the different photocatalysts with and without 4.4 mM of H_2O_2: $SiO_2@WO_3$ (blue), $SiO_2@WO_3@Fe_3O_4$ (red), $SiO_2@WO_3$ with H_2O_2 (navy) and $SiO_2@WO_3@Fe_3O_4$ with H_2O_2 (orange). (b) Degradation of MB aqueous solutions (6×10^{-5} M) reusing the $SiO_2@WO_3@Fe_3O_4$ photocatalyst (1 mg mL^{-1}) and in the presence of H_2O_2 (4.4 mM). (c) Photodegradation of an aqueous DCF solution (1.5×10^{-4} M) under visible-light irradiation (8 lamps of λ_{em} *ca.* 420 nm) in the presence of 1 mg mL^{-1} of $SiO_2@WO_3@Fe_3O_4$ and 11 mM of H_2O_2.

The monoclinic phase of WO_3 is further confirmed in both photocatalysts by Raman spectroscopy (Figure 2d), which shows Raman active modes at 801 cm^{-1}, 710 cm^{-1}, 325 cm^{-1}, and 273 cm^{-1} [44]. The signals found at 801 cm^{-1} and 710 cm^{-1} correspond to the W-O-W stretching modes, while 325 cm^{-1} and 273 cm^{-1} signals correspond to the W-O-W bending modes [45]. The signals corresponding to Fe_3O_4 on $SiO_2@WO_3@Fe_3O_4$ were not observed, nor in Raman spectroscopy or in XRD analysis, probably due to the low content of Fe_3O_4.

Specific surface area (SSA), as a relevant characteristic directly linked with the catalytic activity of heterogeneous materials, was also determined. N_2 adsorption-desorption isotherms (Figure 2e,f) showed a value of 15.2 m^2 g^{-1} for $SiO_2@WO_3$, and of 9.4 m^2 g^{-1} for $SiO_2@$-$WO_3@Fe_3O_4$. The decrease in SSA for $SiO_2@WO_3@Fe_3O_4$ could be due to the partial coverage of WO_3 nanocrystals (*ca.* 7 nm) by the higher Fe_3O_4 nanoparticles (*ca.* 12 nm).

The chemical composition of the surface of $SiO_2@WO_3@Fe_3O_4$ photocatalyst was studied by X-ray photoelectron spectroscopy (XPS). The XPS survey spectra show the presence of Fe2p, O1s, C1s, W4f, and Si2p, respectively (see Figure S8). The high-resolution XPS spectrum of Si2p (see Figure 3a) shows a peak at 103.3 eV, which agrees with the reported one for SiO_2 [46]. The high-resolution W4f spectrum shows peaks at 37.6 and 35.4 eV, which can be assigned to W4f$_{5/2}$ and W4f$_{7/2}$, respectively (see Figure 3b). These peaks correspond to the VI oxidation state of tungsten in WO_3 [47]. Figure 3c shows that a low-resolution peak is achieved for Fe2p$_{3/2}$ due to the low content of Fe_3O_4. Thus, the peaks at 712.1 and 710.2 eV could be attributed to the Fe2p$_{3/2}$ of Fe^{3+} and Fe^{2+} species, respectively [48]. Figure 3d shows the high-resolution O1s spectrum with two peaks at 532.6 and 530.6 eV, corresponding to the oxygen present in SiO_2 and WO_3, respectively [46, 49]. The data of the chemical composition of the surface of $SiO_2@WO_3$ photocatalyst by X-ray photoelectron spectroscopy (XPS) agree with those of $SiO_2@WO_3@Fe_3O_4$ photocatalyst commented above (see Figure S9).

3.2. Photocatalytic activity of $SiO_2@WO_3$ and $SiO_2@WO_3@Fe_3O_4$

The photocatalytic activity of the synthesized $SiO_2@WO_3$ and $SiO_2@WO_3@Fe_3O_4$ photocatalysts was evaluated through the
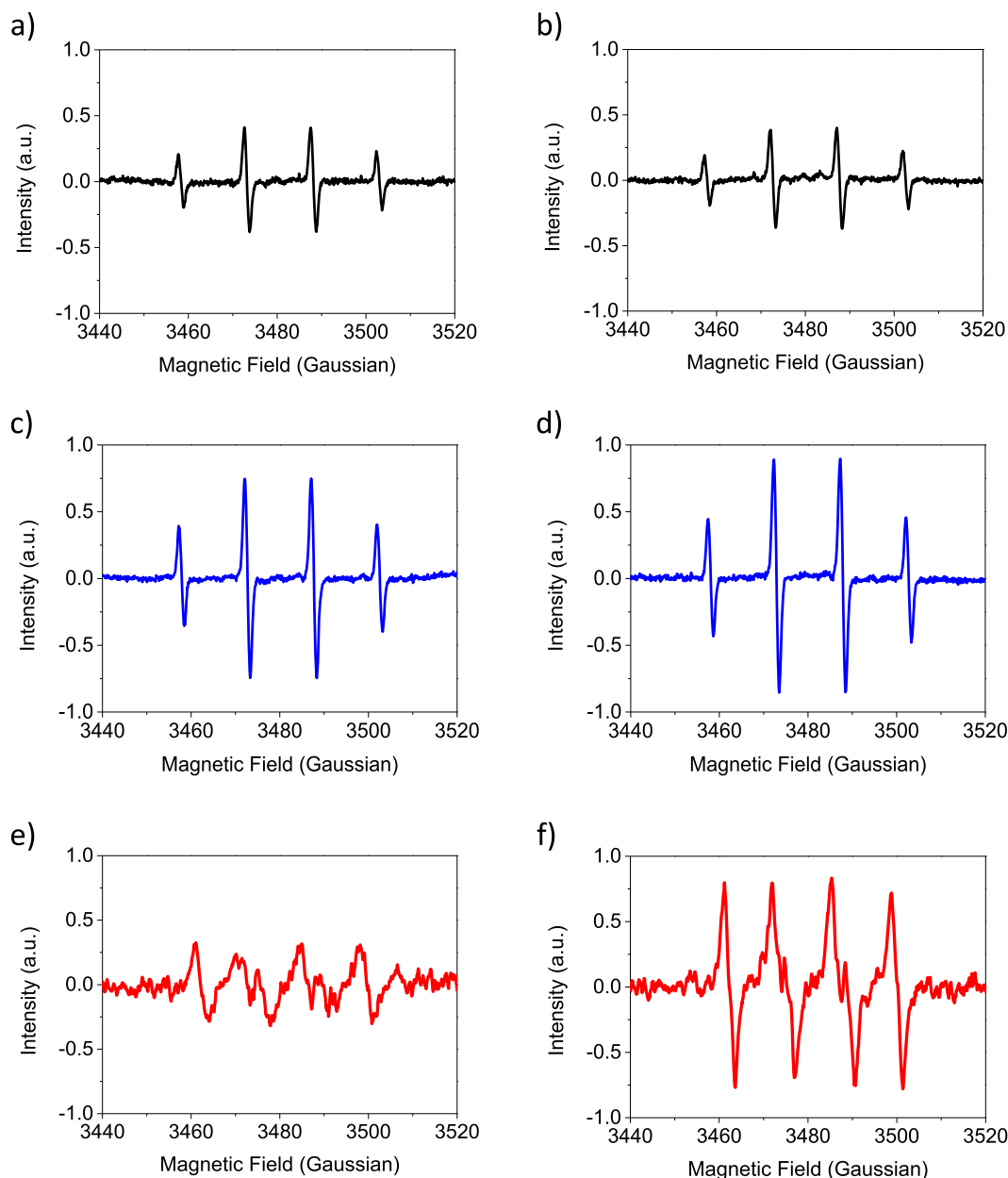
Figure 5. EPR spectra of DMPO (10 mM) solutions irradiated with visible light in the presence of 1 mg mL^{-1} of SiO$_2$@WO$_3$ and SiO$_2$@WO$_3$@Fe$_3$O$_4$ in water (a, b, respectively), in aqueous H$_2$O$_2$ (4.4 mM) (c, d, respectively), in H$_2$O:EtOH (1:4) (e, f, respectively).

degradation of MB as a model contaminant. Hence, when aqueous mixtures of MB (6×10^{-5} M) in the presence of SiO$_2$@WO$_3$ or SiO$_2$@WO$_3$@Fe$_3$O$_4$ (1 mg mL^{-1}) were irradiated under visible light (λ_{max} 420 nm), with and without H$_2$O$_2$ (4.4 M) at pH *ca.* 7, different MB degradation profiles were observed (see Figure 4a). A clear enhancement in the MB photodegradation was observed for both photocatalysts in the presence of H$_2$O$_2$. Even more, the presence of Fe$_3$O$_4$ on SiO$_2$@WO$_3$ (SiO$_2$@WO$_3$@Fe$_3$O$_4$) produced a positive increase in the degradation of MB, resulting in more than 90% degradation after 120 minutes of irradiation (pseudo-first order constant values were 0.018 min^{-1} for SiO$_2$@WO$_3$@Fe$_3$O$_4$ and 0.010 min^{-1} for SiO$_2$@WO$_3$, respectively, both in presence of 4.4 mM of H$_2$O$_2$).

Control experiments such as irradiation of MB solutions in the presence of Fe$_3$O$_4$ (0.06 mg mL^{-1}, which would be approximately the amount of magnetite in 1 mg mL^{-1} of SiO$_2$@WO$_3$@Fe$_3$O$_4$) and H$_2$O$_2$ (4.4 mM), or dark solutions of MB in the presence of SiO$_2$@WO$_3$@Fe$_3$O$_4$ (1 mg mL^{-1}) and H$_2$O$_2$ (4.4 mM), did not produce any MB degradations

during 120 minutes of irradiation (see section S5 in the SI). The insignificant capability of the free nanoparticles of magnetite to produce MB oxidation in the presence of light could be attributed to the low light intensity used. In fact, other studies reported higher degradation of organic pollutants when irradiating similar free Fe$_3$O$_4$ nanoparticles in the presence of H$_2$O$_2$ or WO$_3$ nanomaterials with 10 times fold intensity of light [18,23,29].

The reusability of the SiO$_2$@WO$_3$@Fe$_3$O$_4$ was evaluated by performing four consecutive photocatalytic cycles (see Figure 4b). Results showed that there was not any remarkable decrease in its photocatalytic activity. These results clearly support the high expected stability of the WO$_3$ nanocrystals shell and also that the iron leaching from the magnetite is negligible, which was also evidenced using the 1,10-phenanthroline test, where ferroin (a complex of Fe^{2+} with phenanthroline) was not observed (see details in section S6 in SI). Thereby, there is no MB degradation occurring by Fenton and/or photo Fenton processes from Fe^{2+} leached in the aqueous media.
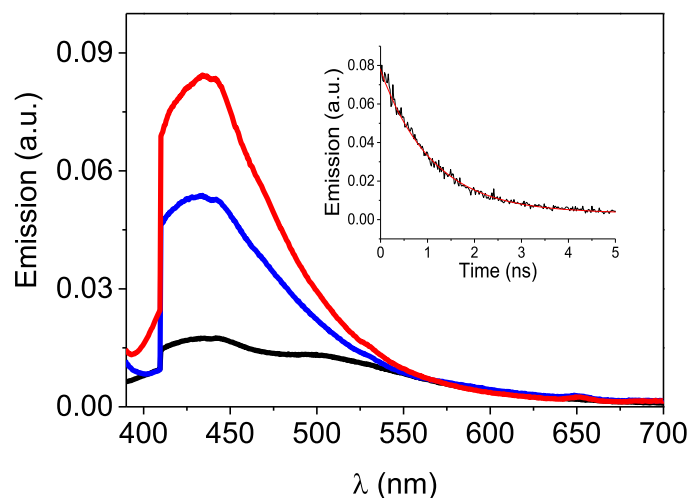
Figure 6. Photoluminescence (PL) emission spectra of Fe_3O_4 (black), $SiO_2@WO_3$ (blue), and $SiO_2@WO_3@Fe_3O_4$ (red) at an excitation wavelength of 366 nm. Inset: PL emission decay lifetime of $SiO_2@WO_3@Fe_3O_4$ at 455 nm (black) and its fitting (red).

With these results, it was decided to evaluate the potential of $SiO_2@WO_3@Fe_3O_4$ photocatalyst for wastewater remediation against the photodegradation of a contaminant of emerging concern like DCF. Thus, the combination of $SiO_2@WO_3@Fe_3O_4$ and H_2O_2 produced the photodegradation of 80 % of DCF (1.5×10^{-4} M) in 180 minutes of visible light irradiation, together with a 34% of decrease of the total organic carbon (Figure 4c). Control experiments showed that DCF is not degraded in the presence of light and H_2O_2 in the absence of the photocatalyst (results not shown).

3.3. Evidence of intermediates generated upon irradiation of the photocatalysts by EPR spectroscopy measurements

For the EPR experiments, 5,5-dimethyl-1-pyrroline-N-oxide (DMPO) was used as a spin trap to detect the potential formation of hydroxyl radical and superoxide radical anion, upon irradiation of the photocatalysts, through the formation of DMPO-OH and DMPO-O_2^- spin adducts, respectively [50]. Thus, when aqueous suspensions of the two photocatalysts were irradiated with DMPO (Figure 5a-d), a four-line EPR signal with 1:2:2:1 intensity with hyperfine coupling constants of a_N = 14.97 G and a_H = 14.77 G was detected, which can be safely associated with the DMPO-OH spin adduct as a piece of evidence for the formation of ·OH [51,52]. Results from the control experiments are shown in Figure S12. It is noteworthy that the presence of H_2O_2 produces a notable DMPO-OH signal increment (see Figure 5a,b vs Figure 5c,d, respectively). Moreover, the intensity of the DMPO-OH signal was higher when using $SiO_2@WO_3@Fe_3O_4$, rather than with $SiO_2@WO_3$.

Additional EPR assays were performed in a mixture of H_2O:EtOH (1:4) as a solvent to increase the probability of detecting $O_2^{·-}$, since EtOH acts as an efficient quencher of ·OH; thus, no formation of DMPO-OH was expected. Thereby, as it can be observed in Figure 5e,f, an EPR signal with hyperfine coupling constants of a_N = 13.42 G, a_H^β = 10.70 G, and a_H^γ = 1.23 G, attributable to the DMPO-O_2^- spin adduct [53] was generated using $SiO_2@WO_3@Fe_3O_4$, and with less intensity also for $SiO_2@WO_3$. The results of the control experiments are shown in Figure S13. The high intensity of the signals detected for $SiO_2@$-$WO_3@Fe_3O_4$ compared to the ones from $SiO_2@WO_3$ can be attributed to the presence of Fe_3O_4, because previous EPR studies have reported the generation of $O_2^{·-}$ from magnetite nanoparticles [23]. In fact, it is well known that reduced iron species are rapidly oxidized by O_2 at near-neutral pH, yielding Fe^{3+} and $O_2^{·-}$ [54].

3.4. Photoluminescence emission properties of the photocatalysts

Photoluminescence (PL) emission spectra of $SiO_2@WO_3$ and $SiO_2@WO_3@Fe_3O_4$ photocatalysts were recorded at the excitation wavelength of 366 nm using Fe_3O_4 nanoparticles as reference. Thus, an emission maximum of *ca.* 440 nm was observed for the three samples (see Figure 6). Besides, the lifetime of the PL emission was 1.10 ns for both photocatalysts ($SiO_2@WO_3$ and $SiO_2@WO_3@Fe_3O_4$).

The PL observed for $SiO_2@WO_3$ photocatalyst is quite similar to the one registered for mesocrystals of WO_3 [55]. However, a higher intensity of PL emission was observed for $SiO_2@WO_3@Fe_3O_4$ compared to $SiO_2@WO_3$. Although it is widely accepted that the higher the PL intensity, the higher the e^-/h^+ recombination and, therefore, the lower the photocatalytic activity, exceptions to this trend have already been reported for other kinds of semiconductors [56,57]. In fact, the participation of the surface, oxygen vacancies, etc, in the observed PL is still under controversy. Furthermore, an anomalous enhancement in photoluminescence emission has been reported for $Fe_3O_4@SiO_2$ core@shell materials [58]. In that case, the authors attributed that increase to the reduction of the non-radiative centers at the interfaces of the core and shell. This effect could be operating in our case. Thus, the lower PL intensity exhibited by $SiO_2@WO_3$ compared to that of $SiO_2@WO_3@Fe_3O_4$ could be attributed to a decrease of non-radiative processes when the Fe_3O_4 nanoparticles are added to the WO_3 surface. Therefore, the expected PL decrease attributable to a reduction of e^-/h^+ recombination processes in $SiO_2@WO_3@Fe_3O_4$ could be masked by the mentioned effect.

3.5. Plausible mechanisms for the photooxidation of organic compounds by $SiO_2@WO_3$ and $SiO_2@WO_3@Fe_3O_4$

After a detailed characterization and evaluation of the performance of the photocatalysts, hydroxyl radical ought to be the reactive species responsible for MB and DCF oxidative photodegradation. Plausible mechanisms to explain the photocatalytic generation of this intermediate from $SiO_2@WO_3$ or $SiO_2@WO_3@Fe_3O_4$, with and without H_2O_2, are shown in Figure 7.

First, as expected, in the absence of H_2O_2, $SiO_2@WO_3$ does not show relevant photoactivity due to the fast recombination of charge carriers (Figure 4a, blue trace). In fact, although the generation of ·OH is thermodynamically feasible from the holes of the VB of WO_3, the reduction potential of the electrons of the CB of WO_3 is, theoretically, insufficient to generate $O_2^{·-}$ from O_2 [15]. In agreement with the observed photoactivity, signals attributable to ·OH were detected by EPR, while the signals corresponding to $O_2^{·-}$ showed very low intensity (Figure 5e). Nevertheless, the addition of H_2O_2 to the reaction media leads to a significant enhancement in the MB photodegradation rate (Figure 4a, navy trace) due to a parallel generation of ·OH from two different pathways. The first pathway involves the reaction of the photogenerated electrons in the CB of WO_3 with H_2O_2 (E_{red}^0 (H_2O_2/·OH) = + 0.80 V vs NHE). This process also reduces the e^-—h^+ pair recombination, enhancing the efficiency of the second pathway: the oxidation of H_2O in the holes of the VB of WO_3 [59]. This proposed mechanism (Figure 7a) is supported by the results obtained from the EPR experiments, where a more intense signal corresponding to DMPO-OH is detected when adding H_2O_2 (Figure 5c *vs* 5a).

Second, when $SiO_2@WO_3@Fe_3O_4$ was used as the photocatalyst in the absence of H_2O_2, the degradation of MB resulted in being only significant during the first few minutes of the irradiation (Figure 4a, red trace). In this case, photogenerated electrons in the CB of WO_3 would be transferred to the CB of magnetite to reduce Fe^{3+} into Fe^{2+}. In fact, the redox potential of CB of magnetite (E_{CB} *ca.* 0.2 V vs NHE), that of the CB of WO_3 (E_{CB} 0.2-0.5 V vs NHE), and the E_{red}^0 (Fe^{3+}/Fe^{2+}) = + 0.77 V vs NHE) are very close (see Figure 7b) [15,60,61]. Thereby, the e^-—h^+ pair recombination is initially prevented, thus ·OH can be generated from the holes of the VB of WO_3. However, the insignificant MB degradation after

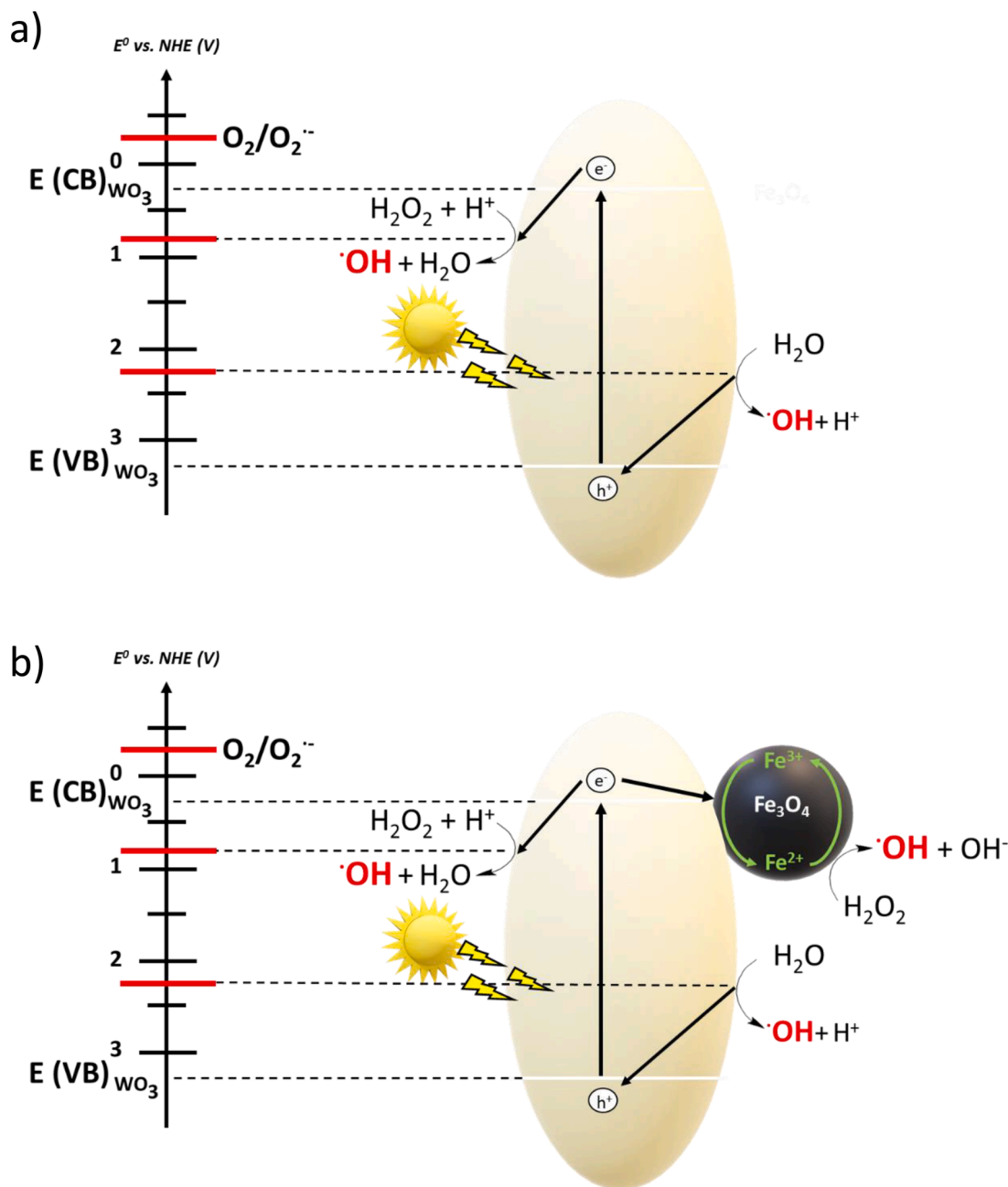**Figure 7.** Hydroxyl radical generation processes involved in the MB degradation produced from visible light excitation of $SiO_2@WO_3$ or $SiO_2@WO_3@Fe_3O_4$ photocatalysts (a and b, respectively) in the presence of H_2O_2.

the first few minutes of irradiation indicates that the ·OH generation would stop when most of the Fe^{3+} of Fe_3O_4 nanoparticles was reduced to Fe^{2+}. As a result, the recombination of the photogenerated electrons in CB of WO_3 with the holes of the VB would be again the main process. Although a photo-Fenton reaction between Fe^{3+} and H_2O to generate Fe^{2+} and ·OH would also be occurring in the magnetite particles, this process must be minor. In fact, control irradiations performed with Fe_3O_4 nanoparticles showed insignificant MB degradation.

Interestingly, the addition of H_2O_2 in the reaction media (Figure 4a, orange trace) using $SiO_2@WO_3@Fe_3O_4$ as photocatalyst produces an even higher MB photodegradation rate than the observed only using $SiO_2@WO_3@Fe_3O_4$ or $SiO_2@WO_3$ plus H_2O_2. Hence, H_2O_2 and Fe_3O_4 must play important roles in the photocatalytic generation of ·OH. Thus, as discussed above, in the presence of only $SiO_2@WO_3@Fe_3O_4$, ·OH generation occurs initially due to the efficient decrease of $e^- h^+$ pair

recombination of WO_3 due to the reduction of Fe^{3+} to Fe^{2+} in the shell of magnetite. Nevertheless, the presence of H_2O_2 in the reaction medium boosts a Fenton reaction ($Fe^{2+} + H_2O_2 \rightarrow Fe^{3+} + ·OH + {}^-OH$), which maintains the cycle Fe^{3+}/Fe^{2+} active, allowing a continuous generation of ·OH from magnetite and from VB of WO_3 (see Figure 7b). The reduction of H_2O_2 by the electrons in the CB of WO_3 could also be taking place as an additional source of ·OH generation in $SiO_2@WO_3@Fe_3O_4$. However, the fact that MB degradation in the presence of H_2O_2 was faster using $SiO_2@WO_3@Fe_3O_4$ than using $SiO_2@WO_3$ must be due to a more efficient electron transfer process from the photoexcited CB of WO_3 to Fe_3O_4 nanoparticles than to H_2O_2. In fact, as can be observed in Figure 7a,b, if the two common ·OH generation processes were also the major pathways in $SiO_2@WO_3@Fe_3O_4$, MB photodegradation reaction rate would be similar for both photocatalysts. Thereby, the combined presence of light and H_2O_2 induces a synergistic effect between Fe_3O_4

and WO_3 that boosts its photocatalytic activity. In this context, same ·OH generation processes ought to be occurring for the DCF photo-degradation and mineralization.

4. Conclusions

New $SiO_2@WO_3@Fe_3O_4$ microparticles were carefully designed and synthesized to obtain a supported WO_3 photocatalyst with improved oxidant properties. Thereby, a homogeneous WO_3 shell formed by WO_3 nanocrystals lower than 7 nm was obtained over SiO_2 cores, and a subsequent fine and homogeneous decoration with Fe_3O_4 nanoparticles linked to the surface of WO_3 photocatalyst gave rise to the final robust and recyclable $SiO_2@WO_3@Fe_3O_4$ photocatalyst. Thereby, after an extensive characterization, the results of the photocatalytic activity of $SiO_2@WO_3@Fe_3O_4$ and $SiO_2@WO_3$ (synthesized as a control) using methylene blue (MB) as a model contaminant in the presence/absence of hydrogen peroxide, have evidenced that hydroxyl radical is the inter-mediate responsible for MB photooxidation. Moreover, all the pathways involved in the generation of this oxidant species from the $SiO_2@WO_3@Fe_3O_4$ photocatalyst have been evaluated. Electron paramagnetic resonance (EPR) experiments further support the proposed mechanism. It should be highlighted that the presence of light and H_2O_2 induces a synergistic effect between Fe_3O_4 and WO_3 that boosts its photocatalytic activity. In fact, this combination has been demonstrated to be effective in the degradation and mineralization of the well-known CEC diclofe-nac. In view of the results achieved and especially considering the inexpensiveness of silica derivatives as supporting substrates for WO_3-based photocatalysts, we believe that this study could be used as the starting point for the development of semiconductor-based photo-catalysts supported on a different type of silica derivatives.

CRediT authorship contribution statement

Ander Diego-Lopez: Investigation, Writing – original draft. **Oscar Cabezuelo:** Investigation. **Alejandro Vidal-Moya:** Methodology, Vali-dation. **M. Luisa Marin:** Conceptualization, Funding acquisition, Proj-ect administration, Supervision, Validation, Writing – review & editing. **Francisco Bosca:** Conceptualization, Funding acquisition, Project administration, Supervision, Validation, Writing – review & editing.

Declaration of Competing Interest

There are no conflicts of interest to declare.

Data availability

Data will be made available on request.

Acknowledgments

Supplementary materials

Supplementary material associated with this article can be found, in the online version, at doi:10.1016/j.apmt.2023.101879.

References

[1] S. Lavrnić, M. Zapater-Pereyra, M.L. Mancini, Water Scarcity and Wastewater Reuse Standards in Southern Europe: Focus on Agriculture, Water Air Soil Pollut. 228 (2017) 251, https://doi.org/10.1007/s11270-017-3425-2.

[2] M. Campinas, R.M.C. Viegas, C.M.M. Almeida, A. Martins, C. Silva, E. Mesquita, M. R. Coelho, S. Silva, V.V. Cardoso, M.J. Benoliel, M.J. Rosa, Powdered activated carbon full-scale addition to the activated sludge reactor of a municipal wastewater treatment plant: Pharmaceutical compounds control and overall impact on the process, J Water Process Eng 49 (2022), 102975, https://doi.org/10.1016/j.jwpe.2022.102975.

[3] L. Lonappan, S.K. Brar, R.K. Das, M. Verma, R.Y. Surampalli, Diclofenac and its transformation products: Environmental occurrence and toxicity - A review, Environ Int 96 (2016) 127–138, https://doi.org/10.1016/j.envint.2016.09.014.

[4] L.A. Pérez-Estrada, S. Malato, W. Gernjak, A. Agüera, E.M. Thurman, I. Ferrer, A. R. Fernández-Alba, Photo-Fenton Degradation of Diclofenac: Identification of Main Intermediates and Degradation Pathway, Environ Sci Technol 39 (2005) 8300–8306, https://doi.org/10.1021/es050794n.

[5] J. Schwaiger, H. Ferling, U. Mallow, H. Wintermayr, R.D. Negele, Toxic effects of the non-steroidal anti-inflammatory drug diclofenac, Aquatic Toxicol 68 (2004) 141–150, https://doi.org/10.1016/j.aquatox.2004.03.014.

[6] M. Patel, R. Kumar, K. Kishor, T. Mlsna, C.U. Pittman, D. Mohan, Pharmaceuticals of Emerging Concern in Aquatic Systems: Chemistry, Occurrence, Effects, and Removal Methods, Chem Rev 119 (2019) 3510–3673, https://doi.org/10.1021/acs.chemrev.8b00299.

[7] H. Gerischer, The impact of semiconductors on the concepts of electrochemistry, Electrochim Acta 35 (1990) 1677–1699, https://doi.org/10.1016/0013-4686(90)87067-C.

[8] S. Malato, J. Blanco, A. Vidal, C. Richter, Photocatalysis with solar energy at a pilot-plant scale: an overview, Appl Catal B 37 (2002) 1–15, https://doi.org/10.1016/S0926-3373(01)00315-0.

[9] D.S. Bhatkhande, V.G. Pangarkar, A.A. Beenackers, Photocatalytic degradation for environmental applications - a review, J Chem Technol Biotechnol 77 (2002) 102–116, https://doi.org/10.1002/jctb.532.

[10] D. Chen, Y. Cheng, N. Zhou, P. Chen, Y. Wang, K. Li, S. Huo, P. Cheng, P. Peng, R. Zhang, L. Wang, H. Liu, Y. Liu, R. Ruan, Photocatalytic degradation of organic pollutants using TiO2-based photocatalysts: A review, J Clean Prod 268 (2020), 121725, https://doi.org/10.1016/j.jclepro.2020.121725.

[11] A. Khanna, V.K. Shetty, Solar light induced photocatalytic degradation of Reactive Blue 220 (RB-220) dye with highly efficient Ag@TiO2 core–shell nanoparticles: A comparison with UV photocatalysis, Sol Energy 99 (2014) 67–76, https://doi.org/10.1016/j.solener.2013.10.032.

[12] E. Coy, K. Siuzdak, I. Grądzka-Kurzaj, S. Sayegh, M. Weber, M. Ziółek, M. Bechelany, I. Iatsunskyi, Exploring the effect of BN and B-N bridges on the photocatalytic performance of semiconductor heterojunctions: Enhancing carrier transfer mechanism, Appl Mater Today 24 (2021), 101095, https://doi.org/10.1016/j.apmt.2021.101095.

[13] B. Ahmed, S. Kumar, A.K. Ojha, P. Donfack, A. Materny, Facile and controlled synthesis of aligned WO3 nanorods and nanosheets as an efficient photocatalyst material, Spectrochim Acta A Mol Biomol Spectrosc 175 (2017) 250–261, https://doi.org/10.1016/j.saa.2016.11.044.

[14] W. Mu, X. Xie, X. Li, R. Zhang, Q. Yu, K. Lv, H. Wei, Y. Jian, Characterizations of Nb-doped WO3 nanomaterials and their enhanced photocatalytic performance, RSC Adv 4 (2014) 36064, https://doi.org/10.1039/C4RA04080E.

[15] J.C. Murillo-Sierra, A. Hernández-Ramírez, L. Hinojosa-Reyes, J.L. Guzmán-Mar, A review on the development of visible light-responsive WO3-based photocatalysts for environmental applications, Chem Eng J Adv 5 (2021), 100070, https://doi.org/10.1016/j.ceja.2020.100070.

[16] M. Bahmani, K. Dashtian, D. Mowla, F. Esmaeilzadeh, M. Ghaedi, Robust charge carrier by Fe3O4 in Fe3O4/WO3 core-shell photocatalyst loaded on UiO-66(Ti) for urea photo-oxidation, Chemosphere 267 (2021), 129206, https://doi.org/10.1016/j.chemosphere.2020.129206.

[17] G.R. Bamwenda, K. Sayama, H. Arakawa, The effect of selected reaction parameters on the photoproduction of oxygen and hydrogen from a WO_3–Fe^{2+}–Fe^{3+} aqueous suspension, J Photochem Photobiol A Chem 122 (1999) 175–183, https://doi.org/10.1016/S1010-6030(99)00026-X.

[18] N.D. Banić, B.F. Abramović, J.B. Krstić, D.V. Šojić Merkulov, N.L. Finčur, M. N. Mitrić, Novel WO3/Fe3O4 magnetic photocatalysts: Preparation, characterization and thiacloprid photodegradation, J Ind Eng Chem 70 (2019) 264–275, https://doi.org/10.1016/j.jiec.2018.10.025.

[19] V. Dutta, S. Sharma, P. Raizada, V.K. Thakur, A.A.P. Khan, V. Saini, A.M. Asiri, P. Singh, An overview on WO3 based photocatalyst for environmental remediation, J Environ Chem Eng 9 (2021), 105018, https://doi.org/10.1016/j.jece.2020.105018.

[20] Z. Feng, Y. Zhu, Q. Zhou, Y. Wu, T. Wu, Magnetic WO3/Fe3O4 as catalyst for deep oxidative desulfurization of model oil, Mater Sci Eng B 240 (2019) 85–91, https://doi.org/10.1016/j.mseb.2019.01.009.

[21] A. Gandon, C. Nguyen, S. Kaliaguine, T. Do, Synthesis of magnetic core@dual shell Fe3O4@SiO2@WO3 nanocatalysts for olefin double bond oxidative cleavage, Can J Chem Eng 99 (2021) 2003–2013, https://doi.org/10.1002/cjce.23931.

[22] H. Khan, M.G. Rigamonti, G.S. Patience, D.C. Boffito, Spray dried TiO2/WO3 heterostructure for photocatalytic applications with residual activity in the dark, Appl Catal B 226 (2018) 311–323, https://doi.org/10.1016/j.apcatb.2017.12.049.

[23] J. Liao, Y. Xu, Y. Zhao, C.-C. Wang, C. Ge, Ag and Fe_3O_4 Comodified WO_{3-x} Nanocomposites for Catalytic Photothermal Degradation of Pharmaceuticals and

Personal Care Products, ACS Appl Nano Mater. 4 (2021) 1898–1905, https://doi.org/10.1021/acsanm.0c03261.

[24] A. Memar, C.M. Phan, M.O. Tade, Photocatalytic activity of WO_3/Fe_2O_3 nanocomposite photoanode, Int J Hydrogen Energy 40 (2015) 8642–8649, https://doi.org/10.1016/j.ijhydene.2015.05.016.

[25] N.T.T. Nguyen, A.Q.K. Nguyen, M.S. Kim, C. Lee, J. Kim, Effect of Fe^{3+} as an electron-transfer mediator on WO_3-induced activation of peroxymonosulfate under visible light, Chem Eng J 411 (2021), 128529, https://doi.org/10.1016/j.cej.2021.128529.

[26] H. Quan, Y. Gao, W. Wang, Tungsten oxide-based visible light-driven photocatalysts: crystal and electronic structures and strategies for photocatalytic efficiency enhancement, Inorg Chem Front 7 (2020) 817–838, https://doi.org/10.1039/C9QI01516G.

[27] P. Shandilya, S. Sambyal, R. Sharma, P. Mandyal, B. Fang, Properties, optimized morphologies, and advanced strategies for photocatalytic applications of WO_3 based photocatalysts, J Hazard Mater 428 (2022), 128218, https://doi.org/10.1016/j.jhazmat.2022.128218.

[28] K. Villa, S. Murcia-López, T. Andreu, J.R. Morante, Mesoporous WO_3 photocatalyst for the partial oxidation of methane to methanol using electron scavengers, Appl Catal B 163 (2015) 150–155, https://doi.org/10.1016/j.apcatb.2014.07.055.

[29] G. Xi, B. Yue, J. Cao, J. Ye, Fe_3O_4/WO_3 Hierarchical Core-Shell Structure: High-Performance and Recyclable Visible-Light Photocatalysis, Chem Eur J 17 (2011) 5145–5154, https://doi.org/10.1002/chem.201002229.

[30] M. Yoon, Y. Oh, S. Hong, J.S. Lee, R. Boppella, S.H. Kim, F. Marques Mota, S.O. Kim, D.H. Kim, Synergistically enhanced photocatalytic activity of graphitic carbon nitride and WO_3 nanohybrids mediated by photo-Fenton reaction and H2O2, Appl Catal B 206 (2017) 263–270, https://doi.org/10.1016/j.apcatb.2017.01.038.

[31] X. Wang, M. Sayed, O. Ruzimuradov, J. Zhang, Y. Fan, X. Li, X. Bai, J. Low, A review of step-scheme photocatalysts, Appl Mater Today 29 (2022), 101609, https://doi.org/10.1016/j.apmt.2022.101609.

[32] M. Minella, G. Marchetti, E. De Laurentiis, M. Malandrino, V. Maurino, C. Minero, D. Vione, K. Hanna, Photo-Fenton oxidation of phenol with magnetite as iron source, Appl Catal B 154–155 (2014) 102–109, https://doi.org/10.1016/j.apcatb.2014.02.006.

[33] L.K.-S. Ng, E.J.-C. Tan, T.W. Goh, X. Zhao, Z. Chen, T.C. Sum, H. Sen Soo, Mesoporous $SiO_2/BiVO_4/CuO$ nanospheres for Z-scheme, visible light aerobic C–N coupling and dehydrogenation, Appl Mater Today 15 (2019) 192–202, https://doi.org/10.1016/j.apmt.2019.01.010.

[34] W. Stöber, A. Fink, E. Bohn, Controlled growth of monodisperse silica spheres in the micron size range, J Colloid Interface Sci 26 (1968) 62–69, https://doi.org/10.1016/0021-9797(68)90272-5.

[35] K. Petcharoen, A. Sirivat, Synthesis and characterization of magnetite nanoparticles via the chemical co-precipitation method, Mater Sci Eng B 177 (2012) 421–427, https://doi.org/10.1016/j.mseb.2012.01.003.

[36] S. Asuha, B. Suyala, X. Siqintana, S. Zhao, Direct synthesis of Fe_3O_4 nanopowder by thermal decomposition of Fe–urea complex and its properties, J Alloys Compd 509 (2011) 2870–2873, https://doi.org/10.1016/j.jallcom.2010.11.145.

[37] J. Ram, R.G. Singh, R. Gupta, V. Kumar, F. Singh, R. Kumar, Effect of Annealing on the Surface Morphology, Optical and and Structural Properties of Nanodimensional Tungsten Oxide Prepared by Coprecipitation Technique, J Electron Mater 48 (2019) 1174–1183, https://doi.org/10.1007/s11664-018-06846-4.

[38] J. Wang, Z. Chen, G. Zhai, Y. Men, Boosting photocatalytic activity of WO_3 nanorods with tailored surface oxygen vacancies for selective alcohol oxidations, Appl Surf Sci 462 (2018) 760–771, https://doi.org/10.1016/j.apsusc.2018.08.181.

[39] N.R. Lugg, G. Kothleitner, N. Shibata, Y. Ikuhara, On the quantitativeness of EDS STEM, Ultramicroscopy 151 (2015) 150–159, https://doi.org/10.1016/j.ultramic.2014.11.029.

[40] A. Fallah Shojaei, A. Shams-Nateri, M. Ghomashpasand, Comparative study of photocatalytic activities of magnetically separable $WO_3/TiO_2/Fe_3O_4$ nanocomposites and TiO_2, WO_3/TiO_2 and TiO_2/Fe_3O_4 under visible light irradiation, Superlattices Microstruct 88 (2015) 211–224, https://doi.org/10.1016/j.spmi.2015.09.014.

[41] J.F. Guayaquil-Sosa, B. Serrano-Rosales, P.J. Valadés-Pelayo, H. de Lasa, Photocatalytic hydrogen production using mesoporous TiO_2 doped with Pt, Appl Catal B 211 (2017) 337–348, https://doi.org/10.1016/j.apcatb.2017.04.029.

[42] F. Wang, C. DiValentin, G. Pacchioni, Rational Band Gap Engineering of WO_3 Photocatalyst for Visible light Water Splitting, ChemCatChem 4 (2012) 476–478, https://doi.org/10.1002/cctc.201100446.

[43] C. Chacón, M. Rodríguez-Pérez, G. Oskam, G. Rodríguez-Gattorno, Synthesis and characterization of WO_3 polymorphs: monoclinic, orthorhombic and hexagonal structures, J Mater Sci Mater Electron 26 (2015) 5526–5531, https://doi.org/10.1007/s10854-014-2053-5.

[44] J. Díaz-Reyes, R. Castillo-Ojeda, M. Galván-Arellano, O. Zaca-Moran, Characterization of WO_3 Thin Films Grown on Silicon by HFMOD, Adv Condens Matter Phys 2013 (2013) 1–9, https://doi.org/10.1155/2013/591787.

[45] K. Christou, D. Louloudakis, D. Vernardou, N. Katsarakis, E. Koudoumas, One-pot synthesis of WO_3 structures at 95°C using HCl, J Solgel Sci Technol 73 (2015) 520–526, https://doi.org/10.1007/s10971-014-3459-5.

[46] F. Rueda, J. Mendialdua, A. Rodriguez, Y.Barbaux R.Casanova, L. Gengembre, L. Jalowiecki, Characterization of Venezuelan laterites by X-ray photoelectron spectroscopy, J Electron Spectros Relat Phenomena 82 (1996) 135–143, https://doi.org/10.1016/S0368-2048(96)03035-6.

[47] A. Katrib, V. Logie, N. Saurel, P. Wehrer, L. Hilaire, G. Maire, Surface electronic structure and isomerization reactions of alkanes on some transition metal oxides, Surf Sci 377–379 (1997) 754–758, https://doi.org/10.1016/S0039-6028(96)01488-4.

[48] Q. Ai, Z. Yuan, R. Huang, C. Yang, G. Jiang, J. Xiong, Z. Huang, S. Yuan, One-pot co-precipitation synthesis of Fe_3O_4 nanoparticles embedded in 3D carbonaceous matrix as anode for lithium ion batteries, J Mater Sci 54 (2019) 4212–4224, https://doi.org/10.1007/s10853-018-3141-3.

[49] C. Cantalini, M.Z. Atashbar, Y. Li, M.K. Ghantasala, S. Santucci, W. Wlodarski, M. Passacantando, Characterization of sol-gel prepared WO_3 thin films as a gas sensor, J Vac Sci Technol A: Vacuum, Surfaces, and Films 17 (1999) 1873–1879, https://doi.org/10.1116/1.581698.

[50] V. Brezová, D. Dvoranová, A. Staško, Characterization of titanium dioxide photoactivity following the formation of radicals by EPR spectroscopy, Res Chem Intermed 33 (2007) 251–268, https://doi.org/10.1163/156856707779238630.

[51] G.R. Buettner, Spin Trapping: ESR parameters of spin adducts 1474 1528V, Free Radic Biol Med 3 (1987) 259–303, https://doi.org/10.1016/S0891-5849(87)80033-3.

[52] J. Soria, M.J. López-Muñoz, V. Augugliaro, J.C. Conesa, Electron spin resonance study of radicals formed during photo-oxidation of phenol on TiO_2, Colloids Surf A Physicochem Eng Asp 78 (1993) 73–83, https://doi.org/10.1016/0927-7757(93)80312-3.

[53] A. Bosnjakovic, S. Schlick, Spin Trapping by 5,5-Dimethylpyrroline- *N* -oxide in Fenton Media in the Presence of Nafion Perfluorinated Membranes: Limitations and Potential, J Phys Chem B 110 (2006) 10720–10728, https://doi.org/10.1021/jp061042y.

[54] L. Emmenegger, D.W. King, L. Sigg, B. Sulzberger, Oxidation Kinetics of Fe(II) in a Eutrophic Swiss Lake, Environ Sci Technol 32 (1998) 2990–2996, https://doi.org/10.1021/es980207g.

[55] D. Wang, J. Sun, X. Cao, Y. Zhu, Q. Wang, G. Wang, Y. Han, G. Lu, G. Pang, S. Feng, High-performance gas sensing achieved by mesoporous tungsten oxide mesocrystals with increased oxygen vacancies, J Mater Chem A Mater 1 (2013) 8653, https://doi.org/10.1039/c3ta11506b.

[56] J. Liqiang, S. Xiaojun, X. Baifu, W. Baiqi, C. Weimin, F. Honggang, The preparation and characterization of La doped TiO_2 nanoparticles and their photocatalytic activity, J Solid State Chem 177 (2004) 3375–3382, https://doi.org/10.1016/j.jssc.2004.05.064.

[57] D.S. Bohle, C.J. Spina, Cationic and Anionic Surface Binding Sites on Nanocrystalline Zinc Oxide: Surface Influence on Photoluminescence and Photocatalysis, J Am Chem Soc 131 (2009) 4397–4404, https://doi.org/10.1021/ja808663b.

[58] S.K. Jana, S. Majumder, B. Satpati, S.K. Mishra, R.K. Srivastava, S. Banerjee, Enhancement of photoluminescence emission and anomalous photoconductivity properties of Fe_3O_4 @SiO_2 core–shell microspheres, RSC Adv 5 (2015) 37729–37736, https://doi.org/10.1039/C5RA03686K.

[59] D.A. Armstrong, R.E. Huie, S. Lymar, W.H. Koppenol, G. Merényi, P. Neta, D. M. Stanbury, S. Steenken, P. Wardman, Standard electrode potentials involving radicals in aqueous solution: inorganic radicals, Bioinorg React Mech. 9 (2013), https://doi.org/10.1515/irm-2013-0005.

[60] U. Kurien, Z. Hu, H. Lee, A.P. Dastoor, P.A. Ariya, Radiation enhanced uptake of Hg0(g) on iron (oxyhydr)oxide nanoparticles, RSC Adv 7 (2017) 45010–45021, https://doi.org/10.1039/C7RA07401H.

[61] K. Sayama, R. Yoshida, H. Kusama, K. Okabe, Y. Abe, H. Arakawa, Photocatalytic decomposition of water into H_2 and O_2 by a two-step photoexcitation reaction using a WO_3 suspension catalyst and an Fe^{3+}/Fe^{2+} redox system, Chem Phys Lett 277 (1997) 387–391, https://doi.org/10.1016/S0009-2614(97)00903-2.